8. "Water resource infrastructure" refers to water source, distribution, and treatment systems. We assume that wherever there is a resident human population or irrigated cropland, there will be a corresponding water infrastructure. Changes in water demand due to population growth and industrialization or in water supply due to climate change will define the vulnerability of water infrastructure and the human population that is dependent on these systems.
9. S. L. Postel *et al.*, *Science* **271**, 785 (1996).
10. United Nations, *Comprehensive Assessment of the Freshwater Resources of the World* (overview document) (World Meteorological Organization, Geneva, 1997).
11. C. J. Vörösmarty, C. A. Federer, A. Schloss, *J. Hydrol.* **207**, 147 (1998).
12. C. J. Vörösmarty, B. Fekete, M. Meybeck, R. Lammers, *Global Biogeochem. Cycles* **14**, 599 (2000).
13. B. M. Fekete *et al.*, *Global, Composite Runoff Fields Based on Observed River Discharge and Simulated Water Balances, Report 22* (World Meteorological Organization–Global Runoff Data Center, Koblenz, Germany, 1999).
14. Data are from the IPCC Data Distribution Centre, Deutsches Klimarechenzentrum (Max-Planck-Institut) in Hamburg, Germany, and the Climatic Research Unit at the University of East Anglia in Norwich, UK. CGCM1GSa1 and HadCM2GSa1 (GSa, ensemble of greenhouse gas plus sulfate aerosol integrations) scenarios were obtained from http://ipcc-ddc.cru.uea.ac.uk/cru_data/datadownload/download_index.html. Scenarios represent a 1% per year increase in CO_2-equivalent forcing and sulfate aerosol dampening. Original data at 3.75° by 3.75° (latitude by longitude) for CGCM1 and at 2.5° by 3.75° for HadCM2 were bilinearly interpolated to 30′ resolution. Monthly forcings were applied to the WBM, and a statistically equivalent daily time step was used to integrate over time and compute water budget variables, including runoff.
15. Simulated water budgets combined with discharge data from several hundred recording stations in (*13*) yielded a mean global runoff of 300 mm year^{-1} or a discharge of 39,300 km^3 year^{-1}; CGCM1/WBM computed respective values of 319 mm year^{-1} and 41,900 km^3 year^{-1}, whereas HadCM2/WBM gave 302 mm year^{-1} and 39,600 km^3 year^{-1}, respectively.
16. The approach taken is that used in climate impact studies on net primary production by VEMAP Members [*Global Biogeochem. Cycles* **9**, 407 (1995)].
17. The values are statistically significant ($P < 1 \times 10^{-6}$) with the Wilcoxon sign test.
18. A 1-km gridded polygon file [*Arc World Supplement*, 1:3 M scale digital map (ESRI, Redlands, CA, 1995)] defined the spatial extent of 242 countries for which country-level population statistics were available (*19*). We defined urban spatial extents as a set of geographically referenced city polygons with demographic data (n = 1858) (*33*) and distributed the remaining country-level urban population evenly across 1-km pixels classified as city lights from remote sensing (*34*). Lacking digital data to the contrary, we distributed rural population uniformly among digitized points representing populated places [*Digital Chart of the World*, 1:1 M scale digital map (ESRI, Redlands, CA, 1993)] falling outside of urban spatial extents. A total of 155 countries simultaneously showed water demand data and discharges greater than zero and fell within our 30′ digitized land mass. The remaining 87 countries were mostly small islands and were not considered. For the contemporary setting, we account for 99.7% of the global population (*19*); 98.4% of the total is assigned water use statistics.
19. *World Resources: A Guide to the Global Environment 1998–99* (World Resources Institute, Washington, DC, 1998).
20. National and sectoral water use statistics were from (*19*). The mean reporting year was 1986, but the range was from 1970 to 1995. National statistics were normalized to year 1985 by applying usage trends recorded in corresponding regional time series (*5*). Domestic water demand was computed on a per capita basis for each country and distributed geographically with respect to the 1-km total population field. Industrial usage was applied in proportion to urban population. Grid-based aggregates at 30′ resolution were then determined for domestic plus industrial water demand.
21. Country-level totals for agricultural water demand were distributed onto 30′ grid cells on the basis of the fraction of each grid cell classified as irrigated land from (*35*) and prorated on the basis of the ratio of unrealized potential evapotranspiration (i.e., the potential minus the estimated actual) to the potential from (*13*). Irrigation-dependent population was determined by proportionally assigning national-level population to the corresponding irrigated areas in each country. We reason that entire national populations (and not simply local farmers and agribusiness) benefit from the food and fiber (destined for domestic or export markets) and income produced from irrigated land. A/Q uses mean annual discharge. These relative water demand estimates are thus conservative and assume highly effective storage of surface water for irrigation, such as through reservoir impoundment. We consider irrigated agriculture because it is a major component of water resource infrastructure that is subject to changes in the availability of net runoff. Rain-fed agriculture falls outside this definition, and we have not treated it here.
22. Rates of increase in water demand to 2025 from regional estimates (*5*) were applied to the 1985 water withdrawal data set. Future changes in population and urban-to-rural ratios (*19*) were used to shift the geography of water demands. The distribution of irrigable lands was fixed to that observed under contemporary conditions. Projected water withdrawals in (*5*) are dependent on water use efficiencies that both increase and decrease for different parts of the world. These estimates were made through extensive consultation of country-level studies and trend analysis based on per unit agricultural, municipal, and industrial water withdrawals; assumptions regarding future technology adoption; and economic capacity to institute efficiency changes.
23. J. Milliman and R. Mei-e, in *Climate Change: Impact on Coastal Habitation*, D. Eisma, Ed. (CRC Press, Boca Raton, FL, 1995), pp. 57–83.
24. S. Postel, *Interciencia* **10**, 290 (1985).
25. P. Gleick, *The World's Water: The Biennial Report on Freshwater Resources (1998–99)* (Island, Washington, DC, 1998).
26. T. Homer-Dixon, *Int. Secur.* **19**, 5 (1994).
27. M. Falkenmark and J. Rockström, *Ambio* **22**, 427 (1993).
28. M. Bonell *et al.*, *Hydrology and Water Management in the Humid Tropics* (Cambridge Univ. Press, Cambridge, 1993).
29. *World Resources: A Guide to the Global Environment 1996–97* (World Resources Institute, Washington, DC, 1996).
30. D. Conway *et al.*, *Ambio* **25**, 336 (1996).
31. K. M. Strzepek *et al*, in *World Water Scenarios: Analyses*, F. R. Rijsberman, Ed. (Earthscan, London, 2000), pp. 120–159.
32. J. C. Rodda, in *Water: A Looming Crisis* (International Hydrological Program, United Nations Educational, Scientific, and Cultural Organization, Paris, 1998).
33. W. Tobler *et al.*, *The Global Demography Project, Technical Report TR-95-6* (National Center for Geographic Information and Analysis, Santa Barbara, CA, 1995).
34. C. Elvidge *et al.*, *Int. J. Remote Sens.* **18**, 1373 (1997).
35. P. Döll and S. Siebert, *A Digital Global Map of Irrigated Areas, Report A9901* (University of Kassel, Kassel, Germany, 1999).
36. P. Gleick, in *World Water Scenarios: Analyses*, F. R. Rijsberman, Ed. (Earthscan, London, 2000), pp. 27–37.

37. Support for this work was through the Institute for the Study of Earth, Oceans, and Space (University of New Hampshire); NASA Earth Observing System (grant NAG5-6137); NSF Division of Atmospheric Sciences (grant ATM-9707953); Office of Polar Programs (grant OPP-9524740); NASA Tropical Rainfall Monitoring Mission (grant NAG5-4785); and the U.S. Department of Energy (DE-FG02-92ER61473). We acknowledge the efforts of B. Fekete and S. Glidden in helping to develop some of the geographically referenced databases used in this study. We also thank three anonymous reviewers for their comments.

2 February 2000; accepted 3 May 2000

Overpressure and Fluid Flow in the New Jersey Continental Slope: Implications for Slope Failure and Cold Seeps

Brandon Dugan* and Peter B. Flemings

Miocene through Pleistocene sediments on the New Jersey continental slope (Ocean Drilling Program Site 1073) are undercompacted (porosity between 40 and 65%) to 640 meters below the sea floor, and this is interpreted to record fluid pressures that reach 95% of the lithostatic stress. A two-dimensional model, where rapid Pleistocene sedimentation loads permeable sandy silt of Miocene age, successfully predicts the observed pressures. The model describes how lateral pressure equilibration in permeable beds produces fluid pressures that approach the lithostatic stress where overburden is thin. This transfer of pressure may cause slope failure and drive cold seeps on passive margins around the world.

Rapid sediment loading (>1 mm year^{-1}) is documented as a source of overpressure (P*, pressure in excess of hydrostatic) in basins around the world (*1*, *2*). A suite of models describe how overpressure is generated during rapid deposition (*3*–*6*). These models quantify the rock properties and sedimentation rates required to generate and maintain overpressure. Mass and volume measurements of wet and dry core samples provide porosity data (*7*) that we use to document overpressures on the New

503 Deike Building, Department of Geosciences, Penn State University, University Park, PA 16802, USA.

*To whom correspondence should be addressed. E-mail: dugan@geosc.psu.edu

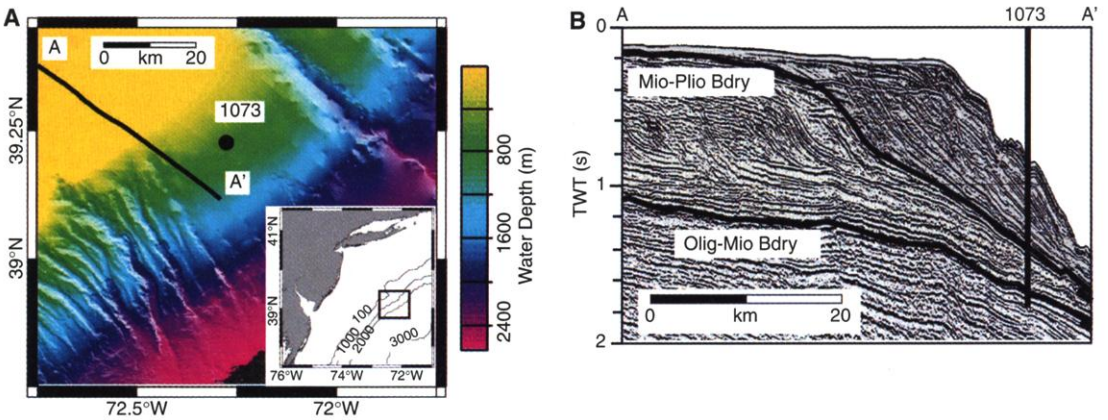

Fig. 1. (**A**) Bathymetric map of the New Jersey continental slope (*41*). ODP (Ocean Drilling Program) Leg 174A Site 1073 is located in 639-m water depth on a smooth portion of the slope (*7*). (**B**) Two-way travel time (TWT) dip seismic line 1002 shows the regional Miocene-Pleistocene stratigraphy (*7*). Black lines identify age boundaries (bdry). In the smooth zone, Pleistocene sediments completely cover the Miocene strata, whereas where canyons are present, the Miocene is exposed (*42*).

Jersey continental slope (Fig. 1). Forward sedimentation models are used to simulate the spatial and temporal evolution of pressure and stress for the slope.

We divide the porosity (ϕ) at Site 1073 into three depth intervals (Fig. 2). Zone 1 extends from the sea floor to 100 mbsf (meters below sea floor), where porosity exponentially decreases from 62 to 45%. Zone 2 is 450 m thick, underlies zone 1, and has constant porosity (ϕ = 45%). Zone 3, the deepest section, begins with an abrupt increase in porosity that is followed by a rapid porosity decrease. These porosity zones may record three distinct pressure regimes: zone 1 is normally compacted and hydrostatically pressured; zone 2 is underconsolidated, overpressured, and has a lithostatic fluid pressure gradient; and zone 3 is underconsolidated, overpressured, and has a hydrostatic fluid pressure gradient.

We quantify this interpretation by coupling porosity and vertical effective stress ($\sigma_v = S_v - \rho_w g z - P^*$) (*2*, *8*).

$$\phi = \phi_o e^{-\beta(S_v - \rho_w g z - P^*)} \quad (1)$$

where ϕ_o is a reference porosity, β is the bulk compressibility, S_v is the overburden, ρ_w is the water density, g is the acceleration due to gravity, and z is the depth below sea surface. This relation is constrained (ϕ_o = 61% and β = 0.44 MPa^{-1}) in zone 1 (*8*–*10*). After constraining β and ϕ_o, Eq. 1 is rearranged and porosity is used to predict overpressure deeper in the section. The regression (Eq. 1) and pressure prediction (Eq. 2) are only performed on clay and silt.

$$P^* = S_v - \frac{1}{\beta}\ln\left(\frac{\phi_o}{\phi}\right) - \rho_w g z \quad (2)$$

In zone 1, where the model was constrained, predicted pressures are hydrostatic. Predicted pressures in zone 2 are 95% of the lithostatic stress (Fig. 2). The predicted pressures at the top of zone 3 approach the lithostatic stress and remain constant at 4.8 MPa through the

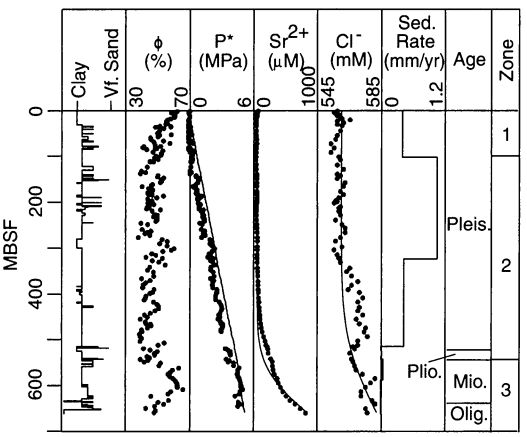

Fig. 2. Core data from ODP Site 1073 (Fig. 1) (*7*). Porosity was determined from wet and dry measurements of mass and volume of core samples. Values denoted by P^* are overpressures predicted from porosity. The solid line on the P^* plot is the reduced lithostatic stress ($S_v - \rho_w g z$). Diffusion modeled Sr^{2+} and Cl^- profiles are solid lines; observations are circles. Pleistocene sedimentation rates far exceeded Miocene and Pliocene sedimentation rates as inferred from biostratigraphic data.

zone. The constant overpressure indicates a hydrostatic fluid pressure gradient in zone 3.

A sedimentation-compaction model (*3*, *11*) is used to simulate the fluid pressure evolution for the New Jersey slope at Site 1073. The model solves Eq. 3 with a finite element approach.

$$\frac{DP}{Dt} = \left[\frac{k(1-\phi)^2}{S_t \mu}\right]\nabla^2 P^* + \left[\frac{\phi\beta}{S_t(1-\phi)}\right]\frac{DS_v}{Dt} \quad (3)$$

where k is the permeability, μ is the fluid viscosity, and S_t is the storage coefficient (*12*, *13*).

The model assumes that sediment loading (DS_v/Dt) is the only source of fluid pressure, the sediments compact according to Eq. 1, and fluid flow follows Darcy's law. The base of the model is a no-flow boundary. The upper boundary (sea floor) is a constant-pressure boundary (P^* = 0). All sediments are deposited with 61% initial porosity (ϕ_o) and with a bulk compressibility (β) equal to 0.44 MPa^{-1} as determined at Site 1073. Compaction is assumed to be irreversible (*14*–*16*). The vertical permeability (k_v) assigned to the Plio-Pleistocene sediments is 1×10^{-18} m^2. The permeability is constrained by experiments on nearby sediments of similar age and lithology (*17*). The model permeability for the Miocene strata is higher ($k_v = 3 \times 10^{-16}$ m^2) than that of the Plio-Pleistocene sediments because they are coarser grained (Fig. 2). The horizontal permeability (k_h) for all sediments is one order of magnitude greater than k_v.

In the one-dimensional (1D) model, the Miocene sediments are assumed to be hydrostatically pressured before they are loaded by the Plio-Pleistocene strata. The modeled Plio-Pleistocene sedimentation rate follows that observed at Site 1073 (Fig. 2). At the end of the Plio-Pleistocene deposition, modeled pressures for zone 1 exceed those predicted from porosity (Fig. 3A). Modeled pressures in zones 2 and 3 reach only 25% of the porosity-predicted pressures (Fig. 3A). To match the porosity-predicted pressures, the model permeability must be decreased by two orders of magnitude. This is representative of a clay and is unrealistically low for the silt-dominated New Jersey slope (*18*, *19*).

In the two-dimensional (2D) model, a 20-km-wide, 0.1-km-thick layer of hydrostatically pressured, permeable Miocene sandy silt is buried for 1 million years by lower permeability Plio-Pleistocene silt and clay (Fig. 3). The model sedimentation rate (DS_v/Dt) de-

creases linearly from the left boundary to the right boundary and varies temporally in agreement with the observations at Site 1073 (Fig. 2).

The 2D model predicts a large lateral flux along the higher permeability Miocene bed, where Darcy velocities reach 7 mm year^{-1} (Fig. 3B). At the toe of the Miocene strata, fluids are expelled laterally and vertically upward with an average Darcy velocity of 0.5 mm year^{-1}. At the left edge of the model domain, where deposition is most rapid, fluids flow slowly (< 0.05 mm year^{-1}) upward to the sea floor and downward to the permeable Miocene section. The shallow Pleistocene sediments (<100 mbsf) have slow flow with Darcy velocities <0.005 mm year^{-1}.

Lateral pressure transfer toward the deltaic toe in the 2D model elevates pressures at Site 1073 relative to the 1D model (Fig. 3A). The 2D model pressures in the Plio-Pleistocene section (zones 1 and 2) are nearly lithostatic. The modeled pressures match the porosity-predicted pressures from 250 to 500 mbsf (Fig. 3A). In zone 3, the model predicts high overpressures (68% of the severe porosity-predicted overpressures) and a hydrostatic gradient (Fig. 3A). The results are consistent with the porosity-predicted pressures and gradients in zones 2 and 3, but the modeled pressures and gradients exceed the porosity-predicted pressures in zone 1 (Fig. 3A). The difference between the model results and pressures predicted from porosity in zone 1 may result from the assumption of constant permeability. The sediments in zone 1 are probably more permeable than the deeper sediments because of their high porosity; this would aid fluid drainage and maintain hydrostatic pressure as is observed. Two effects may control the difference between modeled and porosity-predicted pressures in zone 3. First, the porosity–vertical effective stress behavior inferred from the shallow sediments may not describe the behavior of deeper sediments. A second possible explanation is that the Miocene sediments terminate at or near Site 1073 (Fig. 3B). In this case, the model would predict pressures in zone 3 that are closer to the porosity-predicted pressures.

Sr^{2+} and Cl^- porewater concentrations are greatest in the Oligocene section and decrease upward to modern seawater values (Fig. 2). Brines that originated from dissolution of deeper Jurassic salt may be the source of the high Cl^- concentrations (*20*). Recrystallization or dissolution of Sr-rich carbonates at greater depths may have produced the high Sr^{2+} concentrations in Oligocene porewaters (*20*). We use these data as a geochemical tracer to demonstrate that the present-day concentrations are compatible with the 2D flow model. In a 1D diffusion model, we assumed an initial Oligocene porewater concentration equal to that observed today, and we assumed that the overlying beds have seawater concentrations. Oligocene porewater concentrations are modeled as constant because of the high-concentration sources at depth. Sr^{2+} and Cl^- diffusivities are constant, 9.3×10^{-11} m^2 s^{-1} and 2.5×10^{-10} m^2 s^{-1}, respectively, and are scaled for diffusion in a porous medium (*21*, *22*). The modeled concentrations are less than those observed after 1 million years of diffusion (Fig. 2). The predicted Sr^{2+} concentrations are 50% of those observed from 450 to 550 mbsf, and the Cl^- concentrations are 5% less than those observed from 350 to 500 mbsf. These results suggest that the porewater chemistry is dominated by diffusive mass transport. The Darcy velocities predicted by the 2D flow model may provide the advective transport to account for the difference between the observed and predicted concentrations.

The flow model predicts that lateral flow along permeable pathways will decrease vertical effective stress where overburden is thin. As the vertical effective stress decreases (Fig. 3B), the sediments will become unstable (*23*–*25*). Sediment failure on the lower slope may act as a catalyst to headward erosion, a mechanism that contributes to submarine canyon formation (Fig. 1A) (*26*–*28*). Previous studies suggested that high fluid pressures aided canyon formation (*29*–*31*); however, these studies were neglected because they called on a permeable aquifer that extends hundreds of kilometers across the continental shelf to create artesian conditions on the slope (*32*). This lack of hydraulic connectivity from the shoreline to the slope prevents topographic flow from contributing to the elevated pressures on the slope. Our flow model suggests that the progradation of any low-permeability shelf margin over more-permeable strata will provide a mechanism to focus flow and generate overpressure, slope failure, and slope seeps. Although this is a 2D model, we envision that flow will occur in three dimensions, outward and along-slope toward any zone where the overburden is thin.

The flow model provides an explanation for the origin and distribution of sea-floor seeps. Fluid expulsion would be expected at the toe of the slope where the pressure gradients are high. Seeps and geysers are reported on the lower slope of the New Jersey continental margin (*33*) and in many other rapidly loaded passive margins (*34*, *35*). On the New Jersey slope, these seeps will be greatest within canyons where high-permeability Miocene sediments are exposed. High-flux seeps may themselves contribute to grain-by-grain erosion on the slope and on canyon walls (*31*). Solutes in seep fluids can provide energy sources for biological communities (*36*, *37*).

The observations at Site 1073 and model results for the slope show that the New Jersey slope is overpressured and has low vertical effective stress below 100 mbsf. Recently discovered sea-floor cracks offshore Virginia and North Carolina may represent unstable conditions and low vertical effective stresses near the continental shelf-slope break (*38*). Elevated fluid pressures caused by rapid sediment loading, as we have modeled, may be a mechanism responsible for this slope instability. The model predicts that rapid loading in any basin produces high pressures near the depocenter and that lateral transfer of pressure creates near constant overpressure in permeable lenses. The lateral pressure transfer raises vertical effective stress

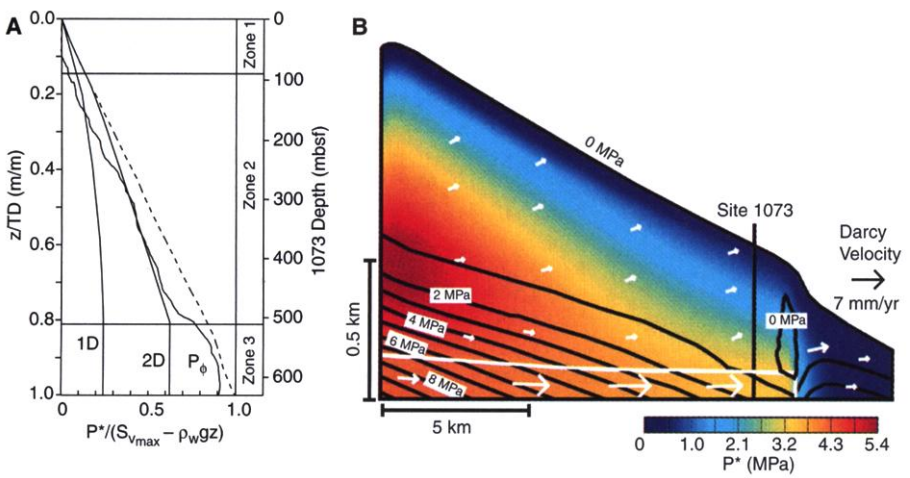

Fig. 3. (**A**) Normalized plot of overpressures for Site 1073. *TD* is the total sediment thickness at Site 1073 and *z* is the distance below the sea floor. The dashed line is the reduced lithostat. Solid lines are one-dimensional model (1D), two-dimensional model (2D), and porosity-predicted (P_ϕ) pressures at Site 1073. Porosity zones and measured depth for Site 1073 are labeled for reference (Fig. 2). (**B**) Simulated 2D vertical effective stress (contour interval = 1 MPa), overpressure (color contours), and flow fields for the New Jersey slope after 1 million years of simulation. The left edge (upper slope) is a no-flow boundary, and the right edge (lower slope) is a constant-pressure boundary ($P^* = 0$). The model geometry is constrained from regional seismic data (Fig. 1B). The white surface is the Miocene-Pliocene boundary. Vertical effective stress is less than 1 MPa for much of the section and is <0 MPa above the toe of the Miocene bed. The low vertical effective stress indicates that the lower slope is at near-failure conditions.

where overburden is thick and decreases vertical effective stress where overburden is thin. These pressure and stress profiles are created solely by differential loading and variations in rock properties (such as permeability and bulk compressibility) and do not require any other mechanism to lower the permeability and increase overpressure (*39*, *40*). The model provides a simple mechanism for overpressure generation and slope failure in basins around the world by providing an explanation for high overpressures that begin at shallow depth on the middle and lower slope. These results revitalize the hypothesis that overpressure contributes to slope geomorphology (*30*–*32*). The lateral flow predicted describes how compaction-driven flow can contribute to the distribution, diversity, and size of cold seeps and the communities that thrive on the solutes in the seep fluids.

References and Notes

1. W. H. Fertl, *Abnormal Formation Pressures* (Elsevier, Amsterdam, 1976), chap. 9.
2. W. W. Rubey and M. K. Hubbert, *Geol. Soc. Am. Bull.* **70**, 167 (1959).
3. R. E. Gibson, *Geotechnique* **8**, 171 (1958).
4. J. D. Bredehoeft and B. B. Hanshaw, *Geol. Soc. Am. Bull.* **79**, 1097 (1968).
5. S. D. Koppula and N. R. Morgenstern, *Can. Geotech. J.* **19**, 260 (1982).
6. C. M. Bethke, *J. Geophys. Res.* **91**, 6535 (1986).
7. J. A. Austin Jr. *et al.*, *Proc. Ocean Drill. Prog. Init. Rep. 174A* (Ocean Drilling Program, College Station, TX, 1998).
8. B. S. Hart, P. B. Flemings, A. Deshpande, *Geology* **23**, 45 (1995).
9. L. F. Athy, *Am. Assoc. Pet. Geol. Bull.* **14**, 1 (1930).
10. A regression of Eq. 1 is performed in zone 1, where P^* is assumed to be zero. Hydrostatic pressures are assumed because the porosity decreases steadily through zone 1 (*8*, *9*). S_v is calculated by integrating the core density. β was also estimated for the Miocene sediments by assuming that they were deposited at hydrostatic conditions. The results provide a β for deep sediments that is similar to that inferred in zone 1. An alternative explanation of the observed porosity-depth signature is that the deeper section is hydrostatically pressured; but the compressibility (β) of the deeper sediments for hydrostatic pressures is only 10% of that of the shallower sediments. We do not believe that rock properties could have changed this significantly within the same effective stress regime and therefore interpret the sediments to be overpressured.
11. D. S. Gordon and P. B. Flemings, *Basin Res.* **10**, 177 (1998).
12. The storage coefficient is defined by $S_s = (\phi\beta)/(1 - \phi) + \phi\beta_f$, and assumes the solid grains are incompressible (*11*). β_f is the fluid compressibility.
13. Eq. 3 is derived in material coordinates and tracks the solid grains during burial.
14. For sediments that are unloading or reloading, the bulk compressibility is assumed to be 0.44×10^{-3} MPa^{-1}.
15. T. W. Lambe and R. V. Whitman, *Soil Mechanics, SI Version* (Wiley, New York, 1979), p. 321.
16. R. F. Craig, *Soil Mechanics* (Chapman & Hall, London, ed. 5, 1992), pp. 83–85.
17. P. Blum, J. Xu, S. Donthireddy, in *Proc. Ocean Drill. Prog. Sci. Results 150*, G. S. Mountain *et al.*, Eds. (Ocean Drilling Program, College Station, TX, 1996), pp. 377–384.
18. O. D. L. Strack, *Groundwater Mechanics* (Prentice Hall, Englewood Cliffs, NJ, 1989), p. 10.
19. C. E. Neuzil, *Water Resources Res.* **30**, 145 (1994).
20. G. S. Mountain *et al.*, *Proc.Ocean Drill. Prog. Init. Rep. 150* (Ocean Drilling Program, College Station, TX, 1994).
21. Y. H. Li and S. Gregory, *Geochim. Cosmochim. Acta* **38**, 703 (1974).
22. P. A. Domenico and F. W. Schwartz, *Physical and Chemical Hydrogeology* (Wiley, New York, 1990), pp. 362–370.
23. K. Terzaghi, *Theoretical Soil Mechanics* (Wiley, New York, 1943), chap. 9.
24. M. K. Hubbert and W. W. Rubey, *Geol. Soc. Am. Bull.* **70**, 115 (1959).
25. P. A. Rona and C. S. Clay, *J. Geophys. Res.* **72**, 2107 (1967).
26. J. M. Robb, J. C. Hampson Jr., D. C. Twichell, *Science* **211**, 935 (1981).
27. B. A. McGregor, W. L. Stubblefield, W. B. F. Ryan, D. C. Twichell, *Geology* **10**, 27 (1982).
28. L. F. Pratson and B. J. Coakley, *Geol. Soc. Am. Bull.* **108**, 225 (1996).
29. D. Johnson, *The Origin of Submarine Canyons* (Hafner, New York, 1967), chap. 4.
30. P. A. Rona, *Am. Assoc. Pet. Geol. Bull.* **53**, 1453 (1969).
31. J. M. Robb, in *Groundwater Geomorphology; The Role of Subsurface Water in Earth-Surface Processes and Landforms*, C. G. Higgins and D. R. Coates, Eds. (Geological Society of America, Boulder, CO, 1990), chap. 12.
32. F. P. Shepard, *Am. Assoc. Pet. Geol. Bull.* **65**, 1062 (1981).
33. P. Rona, R. Sheridan, J. Robb, J. Trotta, F. Grassle, paper presented at the 35th Annual Meeting of the Northeastern Section of the Geological Society of America, New Brunswick, NJ, 13 March 2000.
34. I. R. MacDonald *et al.*, *Geo-Mar. Lett.* **10**, 244 (1990).
35. I. R. MacDonald *et al.*, *Am. Assoc. Pet. Geol. Mem.* **66**, 27 (1996).
36. C. K. Paull *et al.*, *Science* **226**, 965 (1984).
37. K. Olu *et al.*, *Deep-Sea Res. I* **44**, 811 (1997).
38. N. W. Driscoll, J. K. Weissel, J. A. Goff, *Geology* **28**, 407 (2000).
39. H. Kooi, *Basin Res.* **9**, 227 (1997).
40. A. Revil, L. M. Cathles III, J. D. Shosa, *Geophys. Res. Lett.* **25**, 389 (1998).
41. National Geophysical Data Center, www.ngdc.noaa.gov/mgg/bathymetry/hydro.html (1998).
42. J. C. Hampson Jr. and J. M. Robb, *U. S. Geol. Surv. MIS I-1608* (1984).

43. This research would not have been possible without the efforts of M. Malone and the shipboard scientists and staff aboard Leg 174A of the drilling vessel JOIDES *Resolution*. The project was supported by Ocean Drilling Program grant 418925-BA206, NSF grant EAR-9614689, and the Penn State GeoFluids Consortium. B.D. is supported by a Joint Oceanographic Institutions/U.S. Science Advisory Committee Ocean Drilling Fellowship. Geolog (Paradigm) software was used to interpret well data.

23 March 2000; accepted 30 May 2000

Timing the Radiations of Leaf Beetles: Hispines on Gingers from Latest Cretaceous to Recent

Peter Wilf,[1,2]* Conrad C. Labandeira,[2,5] W. John Kress,[3] Charles L. Staines,[4] Donald M. Windsor,[6] Ashley L. Allen,[2] Kirk R. Johnson[7]

Stereotyped feeding damage attributable solely to rolled-leaf hispine beetles is documented on latest Cretaceous and early Eocene ginger leaves from North Dakota and Wyoming. Hispine beetles (6000 extant species) therefore evolved at least 20 million years earlier than suggested by insect body fossils, and their specialized associations with gingers and ginger relatives are ancient and phylogenetically conservative. The latest Cretaceous presence of these relatively derived members of the hyperdiverse leaf-beetle clade (Chrysomelidae, more than 38,000 species) implies that many of the adaptive radiations that account for the present diversity of leaf beetles occurred during the Late Cretaceous, contemporaneously with the ongoing rapid evolution of their angiosperm hosts.

Insects and flowering plants (angiosperms) comprise most terrestrial biodiversity, and their trophic associations are dominant features of terrestrial ecosystems (*1*). Diagnostic insect damage on fossil angiosperms is a primary source of data for understanding the evolution of these associations and can also provide information complementary to insect body fossils on the times of appearance of insect lineages (*2*). Such insect damage is known almost exclusively from dicots (*3*, *4*), although monocots comprise ~22% of living angiosperm species (*5*) and are hosts to diverse groups of herbivorous insects (*6*, *7*). Among the best studied associations between insects and monocots is the specialized feeding of rolled-leaf hispine beetles (family Chrysomelidae, subfamily Hispinae, tribes Cephaloleiini and Arescini) in the semi-

[1]Museum of Paleontology and Department of Geological Sciences, University of Michigan, Ann Arbor, MI 48109–1079, USA. [2]Department of Paleobiology, [3]Department of Botany, [4]Department of Entomology, National Museum of Natural History, Smithsonian Institution, Washington, DC 20560, USA. [5]Department of Entomology, University of Maryland, College Park, MD 20742–4454, USA. [6]Smithsonian Tropical Research Institute, Apartado 2072, Balboa-Ancon, Republic of Panama. [7]Department of Earth and Space Sciences, Denver Museum of Natural History, Denver, CO 80205, USA.

*To whom correspondence should be addressed. E-mail: pwilf@umich.edu